eScience 2 (2022) 79–86

Contents lists available at ScienceDirect

eScience

journal homepage: www.keaipublishing.com/en/journals/escience

Research Paper

Li-rich channels as the material gene for facile lithium diffusion in halide solid electrolytes

Guohao Yang [a,1], Xianhui Liang [a,1], Shisheng Zheng [a], Haibiao Chen [a,b], Wentao Zhang [a], Shunning Li [a,*], Feng Pan [a,*]

[a] School of Advanced Materials, Peking University, Shenzhen Graduate School, Shenzhen, 518055, People's Republic of China
[b] Institute of Marine Biomedicine, Shenzhen Polytechnic, Shenzhen, 518055, People's Republic of China

HIGHLIGHTS

- Seven novel Li-containing halides are identified via simulations to be potential solid electrolytes for Li-ion batteries.
- Facile Li diffusion in halide solid electrolytes is found rooted in the availability of Li-rich channels.
- Li-rich channel is a material gene that can be extended to other electrolyte systems and leveraged for compositional design.

GRAPHICAL ABSTRACT

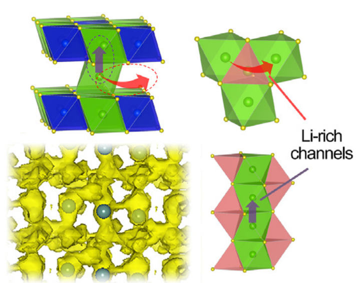

ARTICLE INFO

Keywords:
Li-ion batteries
Inorganic solid electrolytes
Halides
Material gene
Density functional theory

ABSTRACT

Halide solid electrolytes have attracted intense research interest recently for application in all-solid-state lithium-ion batteries. Herein, we present a systematic first-principles study of the Li_3MX_6 (M: multivalent cation; X: halogen anion) halide family that unveils the link between Li-rich channels and ionic conductivity, highlighting the former as a material gene in these compounds. By screening a total of 180 halides for those with high thermodynamic stability, wide electrochemical window, low chemical reactivity, and decent Li-ion conductivity, we identify seven unexplored candidates for solid electrolytes. From these halides and another four prototype compounds, we discover that the facile Li diffusion is rooted in the availability of diffusion pathways which can avoid direct connection with M cations—that is, where the local environment is Li-rich. These findings shed light on strategies for regulating cation and anion frameworks to establish Li-rich channels in the design of high-performance inorganic solid electrolytes.

1. Introduction

The last two decades have seen significantly greater interest in inorganic solid electrolytes (ISEs) for all-solid-state batteries [1–8]. Compared to the liquid organic electrolytes used in conventional lithium-ion batteries (LIBs), which are vulnerable to fire hazards, ISEs have demonstrated transformative advances in mitigating the flammability risk and eliminating the possibility of ionic short circuits [9–11]. However, while there have emerged a number of ISE candidates, none of them appears fully satisfactory. For example, NASICON

* Corresponding author.
E-mail addresses: lisn@pku.edu.cn (S. Li), panfeng@pkusz.edu.cn (F. Pan).
[1] These authors contributed equally.

https://doi.org/10.1016/j.esci.2022.01.001
Received 9 September 2021; Received in revised form 2 December 2021; Accepted 13 January 2022
Available online 22 January 2022

$Li_{1.3}Al_{0.3}Ti_{1.7}(PO_4)_3$ (LATP) [12], garnet $Li_7La_3Zr_2O_{12}$ (LLZO) [13], and perovskite $Li_{3x}La_{2/3-x}\square_{1/3-2x}TiO_3$ [14] are promising oxide ISEs with room-temperature ionic conductivities in the order of 1 mS cm^{-1}. Yet they typically suffer from poor interfacial ion-transfer kinetics due to insufficient contact between particles, which can seriously degrade the overall conductivity [15]. In comparison, sulfide-type ISEs, as represented by $Li_{10}GeP_2S_{12}$ (LGPS) [16] and glass–ceramic $Li_7P_3S_{11}$ [17], are much more ductile, thus enabling intimate contact between grain boundaries and electrode–ISE interfaces. Nevertheless, despite their superior ionic conductivities, these sulfide ISEs are susceptible to electrochemical oxidation when coupled with high-voltage cathodes [18]. Hence, the search for novel ISE materials that satisfy the stringent requirements for high ionic conductivity and electrochemical stability remains one of the top priorities in the design of all-solid-state LIBs.

Recently, a series of Li-containing halides, Li_3MX_6 (M = Sc, Y, Er, In, etc.; X = Cl, Br) [19–26], have demonstrated enormous potential as ISE materials for LIBs, as they possess a wide electrochemical stability window, along with high chemical stability and good ionic conductivity. Computational studies based on density functional theory (DFT) have revealed that sparse cation distribution can endow chloride and bromide ISEs with intrinsically low Li migration energy barriers and excellent electrochemical stability [27,28]. The superionic behavior can be attributed to the following factors: weak binding between the Li ions and anions, abundant vacant sites in the lattice, and a flattened energy landscape due to frustration between the preferred chemical environment and the lattice symmetry [29,30]. With some halide ISEs exhibiting room-temperature ionic conductivities of over 1 mS cm^{-1}, there is a huge opportunity to apply these materials in all-solid-state LIBs [31–33]. However, despite intense efforts to improve the performance of halide ISEs, a comprehensive understanding of how cation and anion frameworks in these compounds affect lithium diffusion remains elusive.

Motivated by the substitutional doping strategies in recent studies [25,34,35], the present work explores compounds in the Li_3MX_6 family (M = Al^{3+}, Ga^{3+}, In^{3+}, Sc^{3+}, Y^{3+}, Mg^{2+}, Ca^{2+}, Sr^{2+}, Zn^{2+}, Ti^{4+}, Zr^{4+}, Hf^{4+}, Ge^{4+}, Sn^{4+}; X = F^-, Cl^-, Br^-) using four structural prototypes: Li_3InCl_6, Li_3YBr_6, Li_3YCl_6, and Li_3AlF_6. These prototypes have previously been demonstrated to exhibit extraordinary Li-ion conductivities. A systematic virtual screening of the Li_3MX_6 compounds via first-principles calculations could facilitate an understanding of high ionic conductivity in specific halides. Through tiered screening regarding stability and Li kinetics, several promising compounds were successfully identified, which exhibited wide electrochemical stability windows, excellent chemical stability against cathode materials, and high lithium-ion conductivities. By analyzing the local environment of the octahedral sites in these structures, we detected the Li-rich channels that proved decisive for facile Li diffusion. The insight into these Li-rich channels, which represented a material gene [36–38] in Li_3MX_6, could be extended to other electrolyte systems and leveraged for the future design of advanced ISEs.

2. Methods

All the DFT calculations were performed using the Vienna ab initio simulation package (VASP) [39] with the projector augmented wave (PAW) [40] method. A plane-wave cutoff energy of 500 eV was adopted, and the Perdew–Burke–Ernzerhof (PBE) exchange-correlation functional was employed. For relaxation and energy calculations, the Brillouin zone was sampled with an $8 \times 4 \times 8$ Γ-centered Monkhorst–Pack (MP) k-point mesh for Li_3InCl_6 and Li_3YBr_6, while $4 \times 4 \times 8$ was used for Li_3YCl_6 and $4 \times 4 \times 4$ for Li_3AlF_6. Since ab initio molecular dynamic (AIMD) simulations are time-consuming, only the gamma point was taken in the Brillouin zone for calculation.

The energy above the convex hull (E_{hull}) indicates the stability of a material against competing stable phases. In this work, if the E_{hull} value is below 25 meV/atom, the halide is considered thermodynamically stable. All grand phase diagrams were built using the python materials genomics (pymatgen) code [41], and the most stable compounds were given as a function of the Li chemical potential. Ordered structures of the mixed-cation compounds were constructed by choosing the configuration with the lowest Ewald energy. Five well-known cathode materials were selected to examine the chemical stability of the halide ISEs against cathodes: $LiCoO_2$, $LiFePO_4$, $LiMn_2O_4$, $LiMnO_2$, and $LiNiO_2$.

Bond valence site energy (BVSE) calculations [42] were used to explore the Li-ion migration paths and to roughly estimate the energy barriers, with the aid of the softBV tool. The precise values of Li-ion conductivity in promising halide ISEs were then calculated using AIMD simulations. An NVT ensemble with a Nose−Hoover thermostat was employed. Mean squared displacement (MSD) data were collected for 40 ps at 800, 900, 1000, 1100, and 1200 K. The time step was set to 2 fs.

3. Theory/calculation

The chemical window was determined using the grand potential phase diagram as a function of the chemical potential of Li:

$$\mu_{Li}(\varphi) = \mu_{Li,0} - e\varphi \tag{1}$$

where $\mu_{Li,0}$ is the chemical potential of lithium metal, e is the elementary charge, and φ is the potential referenced to a lithium metal anode.

The diffusion coefficient (D) was derived from the MSD of Li ions:

$$D = \frac{1}{2Ndt}\sum_{i=1}^{N}\langle|\mathbf{r}_i(t+t_0) - \mathbf{r}_i(t_0)|^2\rangle_{t_0} \tag{2}$$

where N is the total number of Li ions, d is the dimensionality of the system, $\mathbf{r}_i(t_0)$ is the position of the ith ion at initial time t_0, t is the time duration, and the unit in angle brackets is averaged over t_0. The ionic conductivity (σ) was calculated using the Nernst−Einstein equation:

$$\sigma = \frac{(ze)^2 cD}{k_B T} \tag{3}$$

where z is the valence of the ion, e is the elementary charge, c is the concentration of the ion in a unit cell, k_B is the Boltzmann constant, and T is the temperature.

4. Results and discussion

The structures of Li_3InCl_6, Li_3YBr_6, Li_3YCl_6, and Li_3AlF_6 are denoted as T1, T2, T3, and T4, respectively(Fig. 1). Both Li_3InCl_6 and Li_3YBr_6 are monoclinic structure (space group: *C2/m*) based on a face-centered-cubic (FCC) anion sublattice, which is reminiscent of the O3-type $LiTMO_2$ cathodes (TM = Co, Ni, Mn) [43]. Li_3YCl_6 has a hexagonal-close-packed (HCP) anion sublattice with a space group of *P3m1*, while the anion sublattice of Li_3AlF_6 is a mixture of HCP and FCC, with a space group of *C2/c*.

In Li_3InCl_6, Li_3YBr_6, and Li_3YCl_6, the In^{3+}/Y^{3+} and Li^+ ions occupy two-thirds of the six coordinated octahedral interstitial sites in the halogen anion sublattice. The remaining octahedral sites are vacant and can be partially occupied by Li ions during their diffusion, thereby giving rise to a high ionic charge carrier concentration. The above compounds adopt a layered configuration composed of one trivalent cation layer (with or without Li mixing) and one Li layer. In comparison, Li_3AlF_6 displays equivalent distribution of the Al^{3+} cations in all layers, with Al^{3+} ions occupying one-sixth of the octahedral sites of each cation layer. The fluoride ions (F^-) are arranged in an ABACACBCB stacking, exhibiting a lower degree of order than the other structures.

Three substitution strategies were applied to construct potential halide ISEs: (I) substitution with both the trivalent cation (M = Al^{3+}, Ga^{3+}, In^{3+}, Sc^{3+}, Y^{3+}) and the halogen anion (X = F^-, Cl^-, Br^-), for a total of 60 compounds; (II) substitution of the cation with a combination of two different trivalent cations (Al^{3+}, Ga^{3+}, In^{3+}, Sc^{3+}, Y^{3+}), corresponding to a total of 40 compounds; and (III) substitution of the cation

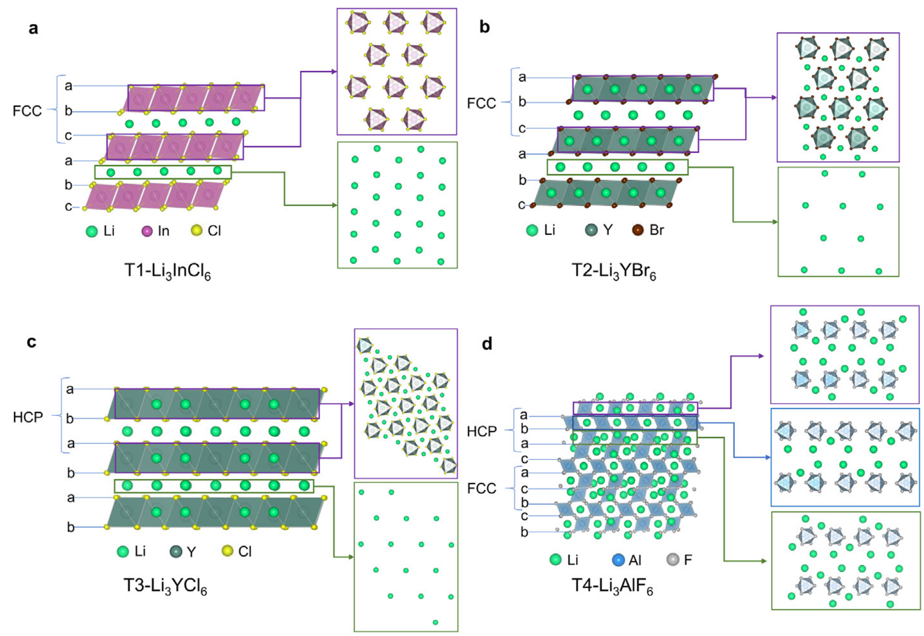

Fig. 1. Structures of the representative halide compounds for ISEs. (**a**) Li_3InCl_6 (denoted as T1). (**b**) Li_3YBr_6 (T2). (**c**) Li_3YCl_6 (T3). (**d**) Li_3AlF_6 (T4). The packing sequence of the anion layers in each compound is also indicated.

with a combination of one divalent cation (Mg^{2+}, Ca^{2+}, Sr^{2+}, Zn^{2+}) and one tetravalent cation (Ti^{4+}, Zr^{4+}, Hf^{4+}, Ge^{4+}, Sn^{4+}), which resulted in a total of 80 compounds. The substitution rule guarantees that all the cations are in their highest valence states. We did not utilize rare-earth elements because of their relatively high price, although good ionic conductivity was shown in halides composed of Er [24,25]. For most of the compounds, the lattice constants experienced only a small degree of change after structural optimization, indicating that their structures were as well preserved as those of the prototypes. Exceptions appeared in the T4 compounds, including Li_3YBr_6, Li_3GaBr_6, Li_3InBr_6, $Li_3Sr_{0.5}Zr_{0.5}F_6$, and $Li_3Sr_{0.5}Hf_{0.5}F_6$, the structures of which experienced relatively significant atomic displacement during structural relaxation, failing to maintain a

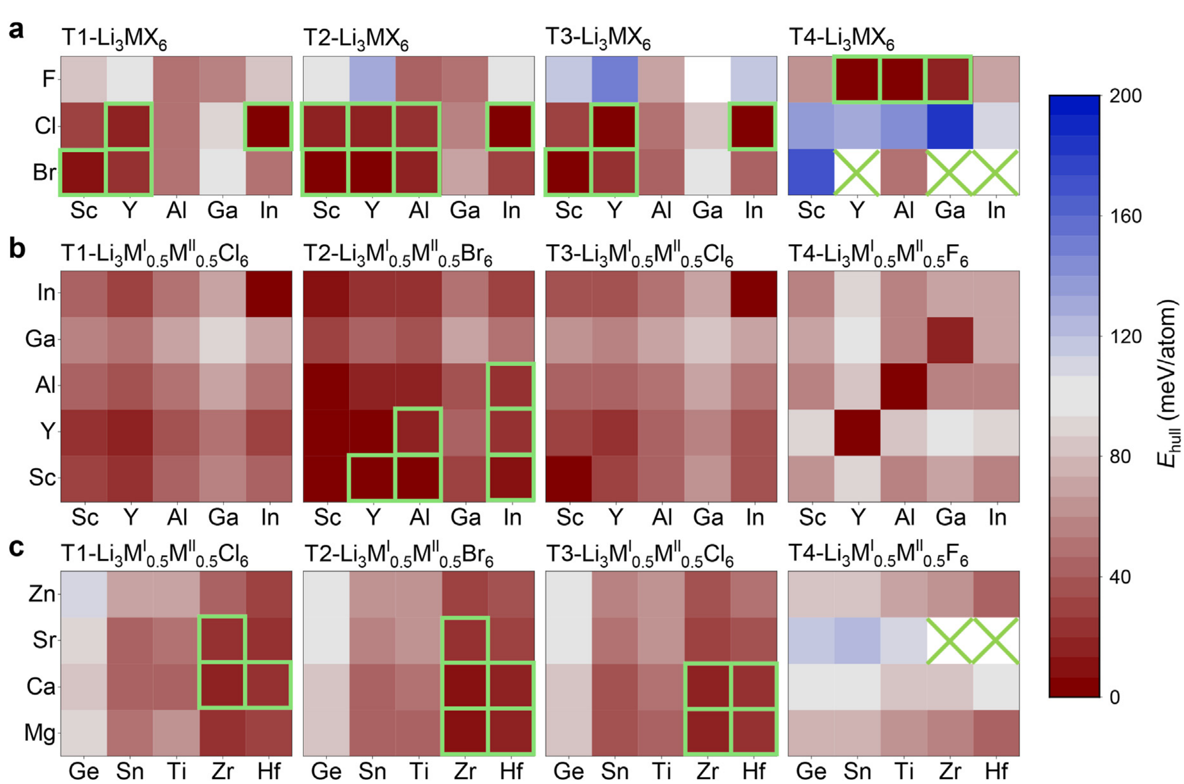

Fig. 2. Energy above hull of the constructed halides. (**a**) Halides obtained by substitution with both the trivalent cation and the halogen anion. (**b**) Halides obtained by substitution of the cation with a combination of two different trivalent cations. (**c**) Halides obtained by substitution of the cation with a combination of one divalent cation and one tetravalent cation. The crossed-out blank squares indicate that the structures collapsed during structural relaxation, while the squares outlined in green highlight the stable compounds, with E_{hull} below 25 meV/atom.

close-packed anion sublattice; consequently, these compounds were not considered in further investigations.

The calculation results for E_{hull} are presented in Fig. 2 and Tables S1–4. Notably, we found 36 compounds to be rather stable, with E_{hull} below 25 meV/atom. Among the three substitution strategies, the highest fraction of stable compounds was produced from strategy I, indicating that substitution with mixed cations is more likely to jeopardize the phase stability than substitution with a single kind of cation in the company of the anion. We also note that a greater number of stable compounds come from the Li_3InCl_6, Li_3YBr_6, and Li_3YCl_6 prototypes than from Li_3AlF_6. This could be due to the relatively low structural symmetry of Li_3AlF_6, which may impose severe structural distortion after element substitution and thereby diminish the stability of the compound.

The 36 thermodynamically stable compounds were selected for further investigation of their electrochemical stability, Li-ion migration energy barrier, and chemical stability. The electrochemical stability window (Fig. 3a) was calculated based on the grand potential phase diagram as a function of Li chemical potential. We set a screening criterion of 2 V, which is close to the corresponding value of T1-Li_3InCl_6. Fourteen new compounds in addition to the four prototypes passed this screening tier. Generally, fluorine-containing structures exhibit a wider electrochemical window than others because of the higher oxidation potential of fluorine, indicating that they are suitable for applications with high-voltage cathodes.

The Li-ion migration energy barriers were preliminarily evaluated via the BVSE model. The calculation results for the activation energy presented in Fig. 3b can provide a prior assessment of the Li diffusion kinetics. We selected 0.4 eV as the screening criterion (blue dashed line). It can be seen that 21 structures exhibit a relatively low energy barrier, meeting the criterion. Among them, 12 compounds also passed the electrochemical stability window criterion: T1-Li_3InCl_6, T1-$Li_3Ca_{0.5}Hf_{0.5}Cl_6$, T2-Li_3YBr_6, T2-Li_3ScBr_6, T2-Li_3ScCl_6, T2-Li_3YCl_6, T2-$Li_3Y_{0.5}Sc_{0.5}Br_6$, T3-Li_3YCl_6, T3-$Li_3Ca_{0.5}Hf_{0.5}Cl_6$, T3-$Li_3Mg_{0.5}Hf_{0.5}Cl_6$, T4-Li_3AlF_6, and T4-Li_3GaF_6. Although BVSE is a simplified empirical method that often overestimates the activation energy, it can serve as an efficient way to conduct tiered screening for Li-ion conductivity [44,45].

The chemical stability was evaluated from the reaction energy between the candidate compounds and five representative cathode materials: $LiCoO_2$, $LiFePO_4$, $LiMn_2O_4$, $LiMnO_2$, and $LiNiO_2$ (Fig. 3c and Table S6). The chemical reaction energies between the candidate halides and $LiNiO_2$ were generally the highest ($>$ 100 meV for all compounds), indicating that most of the halide ISEs are rather unstable when in contact with $LiNiO_2$ and may undergo chemical decomposition at the interface. On the other hand, the chemical reaction energy with $LiFePO_4$ was generally the lowest ($<$ 70 meV for all compounds), indicating that $LiFePO_4$ cathode is especially suitable for assembling full cells with halide ISEs. After excluding T3-$Li_3Ca_{0.5}Hf_{0.5}Cl_6$, which met the electrochemical stability window and Li-ion migration energy barrier criteria but showed high reaction energies with most of the cathode materials, 11 halides remained: the four prototypes (T1-Li_3InCl_6, T2-Li_3YBr_6, T3-Li_3Ycl_6 and T4-Li_3AlF_6) and seven novel compounds — T1-$Li_3Ca_{0.5}Hf_{0.5}Cl_6$, T2-Li_3ScBr_6, T2-Li_3ScCl_6, T2-Li_3YCl_6, T2-$Li_3Y_{0.5}Sc_{0.5}Br_6$, T3-$Li_3Mg_{0.5}Hf_{0.5}Cl_6$ and T4-Li_3GaF_6.

To further evaluate the Li-ion conductivities of these candidates, AIMD simulations were performed at elevated temperatures. The diffusivities of Li ions in the above halide ISEs were derived from the Arrhenius plot given in Fig. 4, and the activation energies are listed in Table 1. Notably, none of these compounds showed melting behavior during simulations (Fig. S1). The activation energies of the four prototype compounds are in good agreement with the literature [20,28,46]. The other seven compounds that have not been examined experimentally all display decent Li-ion conductivities, some of which are even superior to those of the corresponding prototype compounds. It is also noteworthy that all the compounds possess three-dimensional pathways for Li-ion transportation, as evidenced by the Li-ion probability densities shown in Figs. 4e–h. Among these halides, T1-Li_3InCl_6, T2-Li_3ScCl_6, T2-Li_3ScBr_6,

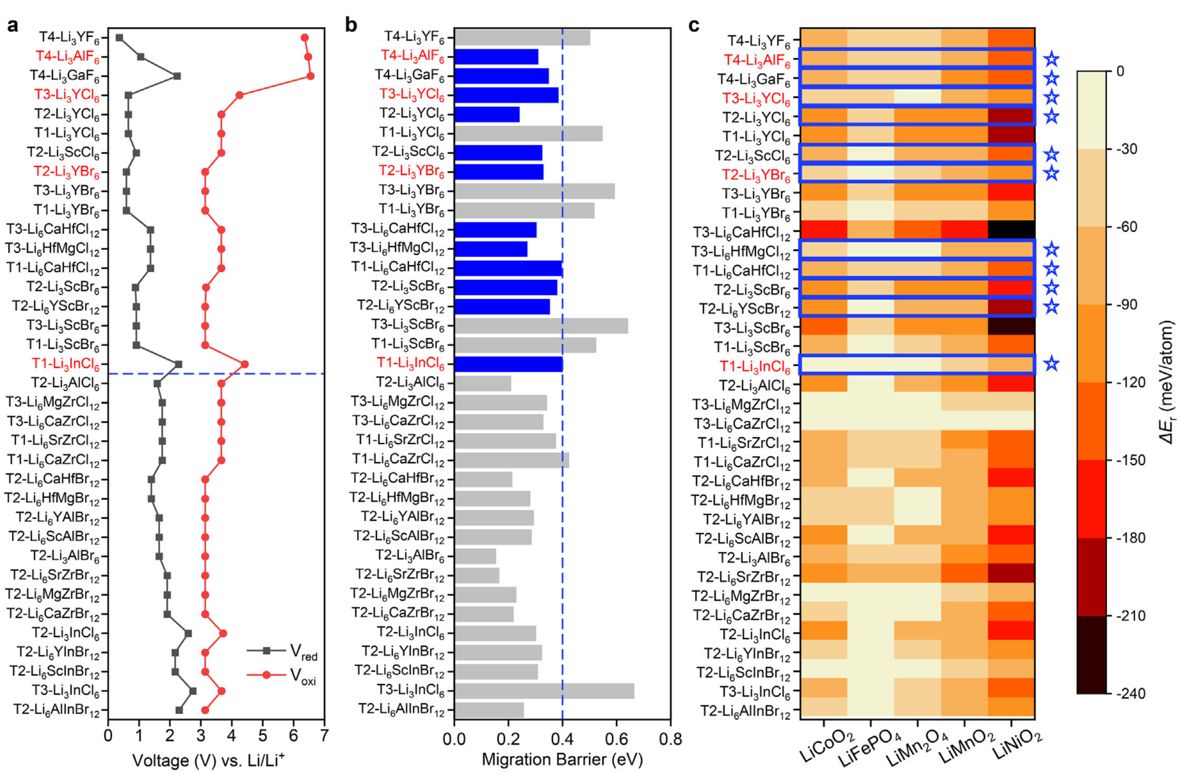

Fig. 3. Screening of 36 candidate halide ISEs. (**a**) Electrochemical stability window. Compounds above the blue dashed line exhibit stability windows wider than 2 V. (**b**) Migration barrier estimated via the BVSE model. The blue dashed line indicates the threshold of 0.4 eV, and candidates that not only meet this screening criteria but also pass the electrochemical stability window screening are highlighted in blue. (**c**) Reaction energy (ΔE_r) with various cathode materials. Halides marked with a star passed all the screening criteria. The red labels indicate the prototype compounds.

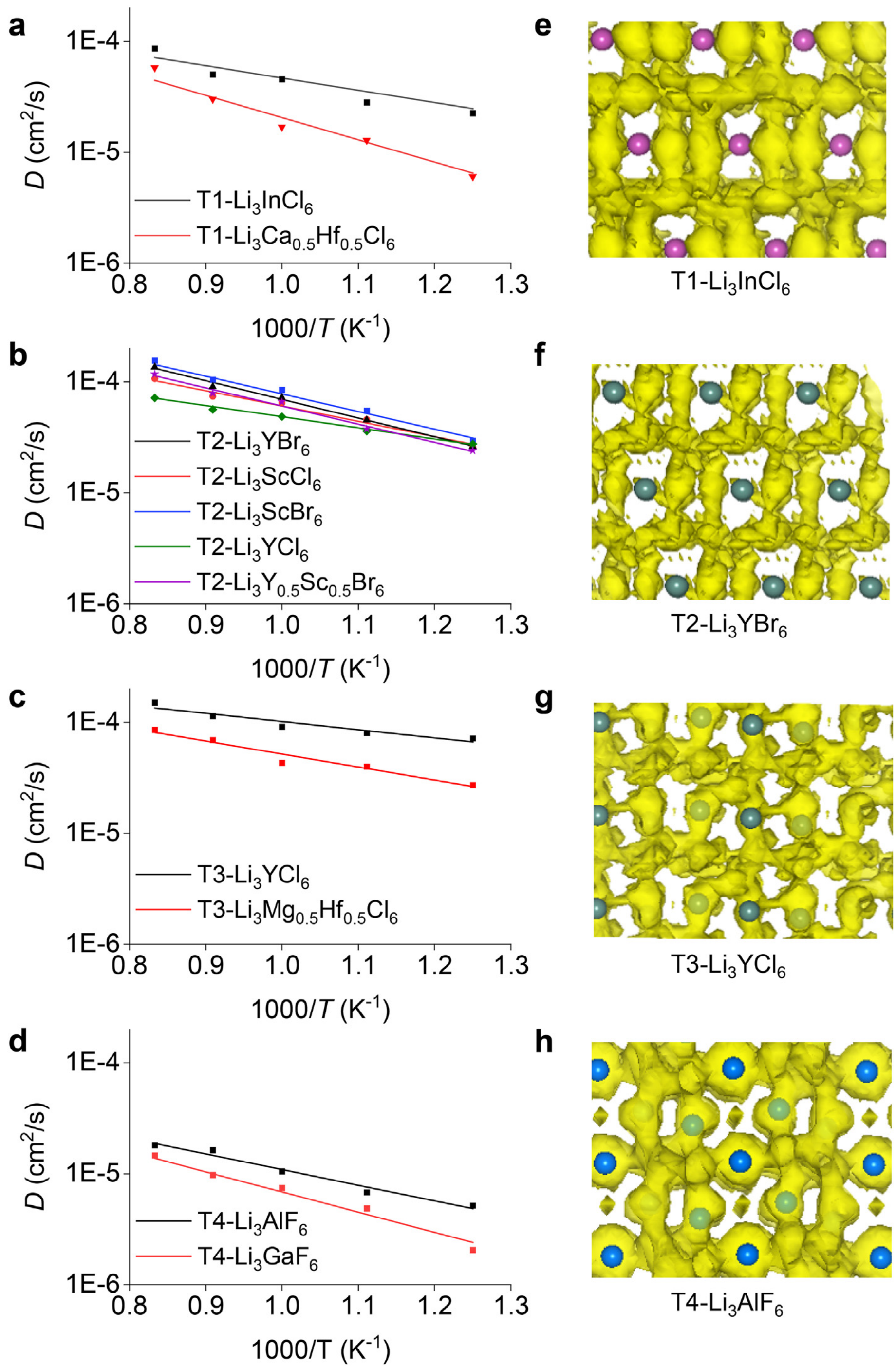

Fig. 4. AIMD simulations for the evaluation of Li-ion conductivity. Arrhenius plot of Li^+ diffusivity of (**a**) T1-, (**b**) T2-, (**c**) T3-, and (**d**) T4-type structures. The Li-ion probability densities in (**e**) T1-Li_3InCl_6, (**f**) T2-Li_3YBr_6, (**g**) T3-Li_3YCl_6, and (**h**) T4-Li_3AlF_6. The yellow surface corresponds to the ionic conduction path.

T2-Li_3YCl_6, T3-Li_3YCl_6, T3-$Li_3Mg_{0.5}Hf_{0.5}Cl_6$, and T4-Li_3AlF_6 can reach a conductivity of up to 1 mS cm^{-1}.

Although the structures of these halide compounds adopt a layered configuration, Li-ion diffusion is not confined to the two-dimensional plane, because a number of vacant sites exist in the M-cation layers. This Li-rich feature can lead to the emergence of special diffusion channels that differ from those in typical layered compounds (Fig. 5). If the anions are arranged in an FCC lattice, Li diffusion will occur through the octahedral-tetrahedral-octahedral (Oct-Tet-Oct) paths [47]. Each of these Oct sites is neighbored by eight Tet sites, while each Tet site shares faces with four Oct sites. Given the relatively confined space of the Tet sites, Li ions accommodated therein will correspond to stronger electrostatic interaction and thus higher site energy than in the Oct sites. A smaller energy difference between Li located at both sites is therefore conducive to flattening the energy landscape for Li diffusion and improving the Li kinetics. Since the stability of Li at a Tet site can be significantly impaired by the electrostatic repulsion from a multivalent M cation occupying one of its neighboring Oct sites [48,49], it is desirable for all of these Oct sites to be either vacant or occupied only by Li. In this case, the nearby Oct sites around this diffusion channel are free of M cations, which can be defined as a “Li-rich” environment. The corresponding pathway is the Li-rich channel. Without M cations in the neighborhood, the anions are less polarized, thus facilitating the charge density redistribution necessary for Li migration [29]. If the anions are in

Table 1
Activation energies and Li-ion conductivities of the candidate halide ISEs.

Candidate	Activation energy (eV)	Conductivity (S cm^{-1})
T1-Li_3InCl_6	0.22 ± 0.02	1.0 × 10^{-2}
T1-$Li_3Ca_{0.5}Hf_{0.5}Cl_6$	0.40 ± 0.04	4.0 × 10^{-5}
T2-Li_3YBr_6	0.33 ± 0.02	5.0 × 10^{-4}
T2-Li_3ScCl_6	0.27 ± 0.04	3.0 × 10^{-3}
T2-Li_3ScBr_6	0.32 ± 0.02	1.0 × 10^{-3}
T2-Li_3YCl_6	0.20 ± 0.02	1.7 × 10^{-2}
T2-$Li_3Y_{0.5}Sc_{0.5}Br_6$	0.32 ± 0.05	5.8 × 10^{-4}
T3-Li_3YCl_6	0.15 ± 0.01	4.4 × 10^{-2}
T3-$Li_3Mg_{0.5}Hf_{0.5}Cl_6$	0.23 ± 0.01	7.4 × 10^{-3}
T4-Li_3AlF_6	0.28 ± 0.03	1.0 × 10^{-3}
T4-Li_3GaF_6	0.36 ± 0.02	8.0 × 10^{-5}

the HCP lattice, a direct Oct–Oct diffusion pathway will emerge, where two Oct sites share a common face (Fig. 5c). This path is also distant from M cations and thus can promote Li-ion diffusion, serving as another Li-rich channel that contributes to high ionic conductivity.

Fig. 6a illustrates the local environments of two different Oct sites in T1-Li_3InCl_6, denoted by Oct-1 and Oct-2. Six out of the eight Tet sites around Oct-1 have one face-sharing M ion, while the remaining two are surrounded only by Li, corresponding to Li-rich channels. In comparison, around the Oct-2 site appear four Li-rich channels. A higher fraction of Li staying at Oct-2 sites means a better chance of transportation through Li-rich channels, in which facile diffusion of Li ions can be anticipated. Here, we define the site occupancy of Li ions as $\alpha = <N_{Li}>/N_{total}$, where N_{total} is the total number of the selected sites per unit cell and $<N_{Li}>$ is the average number of Li per unit cell at these sites over the simulation time. Due to the close-packed nature (FCC or HCP) of the anions, the total number of Oct sites in the lattice is equal to the number of anion atoms, while the number of Tet sites is double that of Oct. $<N_{Li}>$ is counted inside a sphere with a radius equal to the shortest Li-X bond length, and this number is averaged over all the configurations in the simulation.

In Fig. 6b, we provide the results for T2-Li_3YBr_6, whose anion sublattice also exhibits an FCC structure. The local topological environments of the Oct-1 and Oct-2 sites in T2-Li_3YBr_6 are identical to those in T1-Li_3InCl_6. We note that the site occupancy at Oct-2 in T1-Li_3InCl_6 is considerably higher than in T2-Li_3YBr_6, which is very consistent with the better Li-ion conductivity in the former (Table 1). This result indicates that the accessibility of Li to Li-rich channels is a critical factor determining the Li kinetics in halide ISEs.

When the anions are arranged in HCP arrays, as exemplified by T3-Li_3YCl_6 in Fig. 6c, the direct Oct–Oct pathway can penetrate the whole lattice (across the Oct-1 and Oct-2 sites). This can potentially boost Li kinetics in the direction perpendicular to the cation layers. Moreover, all of the six Tet sites around Oct-3 are away from M cations, which may account for the higher site occupancy at the Tet sites than in T1-Li_3InCl_6 and T2-Li_3YBr_6. Despite the existence of direct Oct–Oct channels in T4-Li_3AlF_6 (Fig. 6d), they cannot build a complete fast lane in the compound; that is, to achieve long-range diffusion, Li has to travel through an Oct-Tet-Oct channel after passing a direct Oct–Oct channel (Fig. S2). This implies a less significant role for direct Oct–Oct channels in T4-Li_3AlF_6.

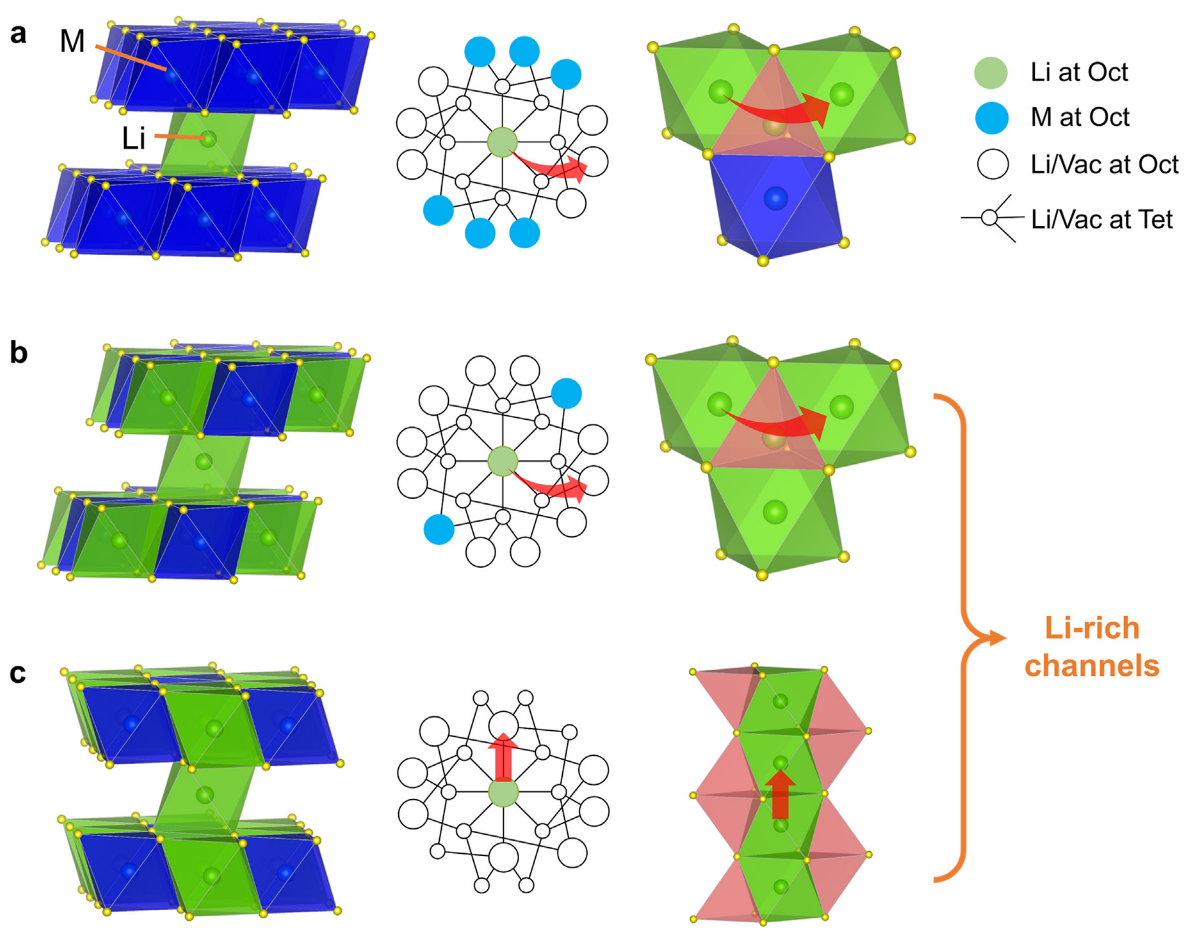

Fig. 5. Li diffusion channels in different structures. **(a)** Typical layered materials, in which multivalent cations (M) occupy all the octahedral sites in one cation layer. **(b)** FCC-type and **(c)** HCP-type layered structures with multivalent cations occupying one-third of the octahedral sites in one cation layer. The middle and right panels illustrate the local environments of an octahedral Li and its diffusion paths to another octahedral site. A linkage between the circles means a face-sharing connection between the corresponding coordination polyhedra in the structure.

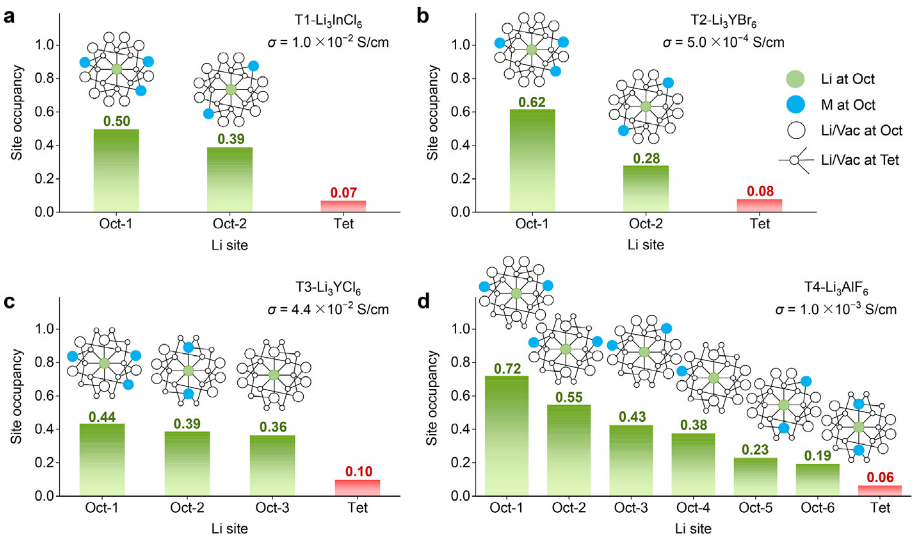

Fig. 6. Average Li occupancy probability in different octahedral and tetrahedral sites. (**a**) T1-Li_3InCl_6. (**b**) T2-Li_3YBr_6. (**c**) T3-Li_3YCl_6. (**d**) T4-Li_3AlF_6. All the configurations are extracted from the AIMD simulations at 1200 K. Insets above the bar illustrate the local structure and connection relations of different sites.

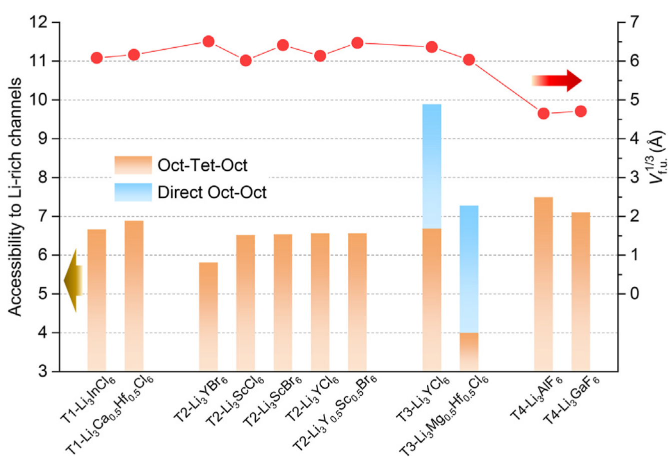

Fig. 7. Accessibility of Li ions to the Li-rich channels, and the cube root of volume per formula unit for different halides. The accessibility to Li-rich channels is derived according to the site occupancy of Li at Oct sites and the available Li-rich channels originating from these sites.

The accessibility of Li ions to the Li-rich channels in Li_3MX_6 can be quantified by the following equation:

$$S = \frac{1}{n_M} \sum_{i}^{N_{Oct}} \alpha_i t_i \tag{4}$$

where α_i is the site occupancy of Li ions at the ith Oct site in the unit cell of the compound; t_i is the number of Tet/Oct sites that face-share with the ith Oct site and can provide Li-rich channels; and N_{Oct} and n_M are the number of Oct sites and the number of M cations per unit cell, respectively. The calculated results obtained from AIMD simulations are shown in Fig. 7. Notably, only T3 structures possess direct Oct–Oct channels that correspond to fast Li^+ diffusion lanes throughout the compound, thus making a considerable contribution to the histogram. In T3-Li_3YCl_6, which gives the highest ionic conductivity, Li ions are more likely to diffuse through the Li-rich channels than in other halides. The lower S values presented by T1-and T2-type structures can be ascribed to the absence of direct Oct–Oct channels. We note that the T4-type halides with small ions (Al^{3+}, Ga^{3+}, F^-) are relatively more compact than other structures, as demonstrated by the cube root of the volume per formula unit ($V_{f.u.}^{1/3}$) displayed in Fig. 7. As a result, the bottleneck at the gate site will be quite narrow [50,51], implying sluggish Li diffusion. However, their performance is actually competitive with some of the T1-and T2-type halides, which most likely originates from higher accessibility to the Li-rich channels. Overall, the above results suggest that the Li-rich channels are an indispensable factor for predicting the Li kinetics in Li_3MX_6 halides, so they can be regarded as a material gene that regulates the desired properties in the company of other critical structural features.

5. Conclusions

In summary, leveraging high-throughput DFT calculations, we have performed a systematic study of halide solid electrolytes based on a portfolio of 180 compounds derived via chemical substitution in four prototype structures (Li_3InCl_6, Li_3YBr_6, Li_3YCl_6, and Li_3AlF_6). Along with these prototypes, seven compounds (T1-$Li_3Ca_{0.5}Hf_{0.5}Cl_6$, T2-Li_3ScBr_6, T2-Li_3ScCl_6, T2-Li_3YCl_6, T2-$Li_3Y_{0.5}Sc_{0.5}Br_6$, T3-$Li_3Mg_{0.5}Hf_{0.5}Cl_6$, and T4-Li_3GaF_6) were identified as having high thermodynamic stability, wide electrochemical stability window, low chemical reactivity, and acceptable Li-ion conductivity. By inspecting the Li-diffusion paths in these structures, we demonstrated the crucial role of Li-rich channels that can mitigate the negative influence of multivalent M cations on Li migration. This characteristic can be regarded as a material gene that distinguishes the Li_3MX_6 halide family from many other Li-containing materials. The new understanding developed in this work highlights that the compositional design of ISEs can be directed towards harnessing the cation and anion sublattices to establish and connect Li-rich channels.

Author contributions

F. Pan, S.N. Li, and G.H. Yang proposed the concept. G.H. Yang, X.H. Liang, and W.T. Zhang performed the data acquisition. H.B. Chen and S.S. Zheng assisted in data analysis. G.H. Yang, S.S. Zheng, and S.N. Li co-wrote the manuscript. F. Pan provided administrative support. All authors participated in manuscript discussions.

Declaration of competing interest

The authors declare that they have no known competing financial interests or personal relationships that could have appeared to influence the work reported in this paper.

Acknowledgments

This work was financially supported by Soft Science Research Project of Guangdong Province (No. 2017B030301013), the Chemistry and Chemical Engineering Guangdong Laboratory (Grant No.1922018), and Shenzhen Science and Technology Research Grant (No. GXWD20201231165807007-20200807111854001).

Appendix A. Supplementary data

Supplementary data to this article can be found online at https://doi.org/10.1016/j.esci.2022.01.001.

References

[1] M. Li, J. Lu, Z. Chen, K. Amine, 30 years of lithium-ion batteries, Adv. Mater. 30 (2018), 1800561.
[2] T. Krauskopf, F.H. Richter, W.G. Zeier, J.R. Janek, Physicochemical concepts of the lithium metal anode in solid-state batteries, Chem. Rev. 120 (2020) 7745–7794.
[3] J.C. Bachman, S. Muy, A. Grimaud, H.H. Chang, N. Pour, S.F. Lux, O. Paschos, F. Maglia, S. Lupart, P. Lamp, Inorganic solid-state electrolytes for lithium batteries: mechanisms and properties governing ion conduction, Chem. Rev. 116 (2016) 140–162.
[4] Y. Xiao, Y. Wang, S.H. Bo, J.C. Kim, L.J. Miara, G. Ceder, Understanding interface stability in solid-state batteries, Nat. Rev. Mater. 5 (2020) 105–126.
[5] J.F. Wu, R. Zhang, Q.F. Fu, J.S. Zhang, X.Y. Zhou, P. Gao, C.H. Xu, J. Liu, X. Guo, Inorganic solid electrolytes for all-solid-state sodium batteries: fundamentals and strategies for battery optimization, Adv. Funct. Mater. 31 (2021), 2008165.
[6] M. Li, C. Wang, Z. Chen, K. Xu, J. Lu, New concepts in electrolytes, Chem. Rev. 120 (2020) 6783–6819.
[7] A. Manthiram, X. Yu, S. Wang, Lithium battery chemistries enabled by solid-state electrolytes, Nat. Rev. Mater. 2 (2017) 16103.
[8] Z. Zou, Y. Li, Z. Lu, D. Wang, Y. Cui, B. Guo, Y. Li, X. Liang, J. Feng, H. Li, C.W. Nan, M. Armand, L. Chen, K. Xu, S. Shi, Mobile ions in composite solids, Chem. Rev. 120 (2020) 4169–4221.
[9] X.B. Cheng, C.Z. Zhao, Y.X. Yao, H. Liu, Q. Zhang, Recent advances in energy chemistry between solid-state electrolyte and safe lithium-metal anodes, Inside Chem. 5 (2019) 74–96.
[10] J. Janek, W.G. Zeier, A solid future for battery development, Nat. Energy 1 (2016) 1–4.
[11] P. Balakrishnan, R. Ramesh, T.P. Kumar, Safety mechanisms in lithium-ion batteries, J. Power Sources 155 (2006) 401–414.
[12] H. Aono, E. Sugimoto, Y. Sadaoka, N. Imanaka, G.y. Adachi, Ionic conductivity of solid electrolytes based on lithium titanium phosphate, J. Electrochem. Soc. 137 (1990) 1023.
[13] R. Murugan, V. Thangadurai, W. Weppner, Fast lithium ion conduction in garnet-type $Li_7La_3Zr_2O_{12}$, Angew. Chem. Int. Ed. 46 (2007) 7778–7781.
[14] S. Stramare, V. Thangadurai, W. Weppner, Lithium lanthanum titanates: a review, Chem. Mater. 15 (2003) 3974–3990.
[15] R. Chen, Q. Li, X. Yu, L. Chen, H. Li, Approaching practically accessible solid-state batteries: stability issues related to solid electrolytes and interfaces, Chem. Rev. 120 (2019) 6820–6877.
[16] N. Kamaya, K. Homma, Y. Yamakawa, M. Hirayama, R. Kanno, M. Yonemura, T. Kamiyama, Y. Kato, S. Hama, K. Kawamoto, A lithium superionic conductor, Nat. Mater. 10 (2011) 682–686.
[17] Y. Seino, T. Ota, K. Takada, A. Hayashi, M. Tatsumisago, A sulphide lithium super ion conductor is superior to liquid ion conductors for use in rechargeable batteries, Energy Environ. Sci. 7 (2014) 627–631.
[18] W.D. Richards, L.J. Miara, Y. Wang, J.C. Kim, G. Ceder, Interface stability in solid-state batteries, Chem. Mater. 28 (2016) 266–273.
[19] T. Asano, A. Sakai, S. Ouchi, M. Sakaida, A. Miyazaki, S. Hasegawa, Solid halide electrolytes with high lithium-ion conductivity for application in 4 V class bulk-type all-solid-state batteries, Adv. Mater. 30 (2018), 1803075.
[20] X. Li, J. Liang, N. Chen, J. Luo, K.R. Adair, C. Wang, M.N. Banis, T.K. Sham, L. Zhang, S. Zhao, Water-mediated synthesis of a superionic halide solid electrolyte, Angew. Chem. Int. Ed. 131 (2019) 16579–16584.
[21] X. Li, J. Liang, J. Luo, M.N. Banis, C. Wang, W. Li, S. Deng, C. Yu, F. Zhao, Y. Hu, Air-stable Li_3InCl_6 electrolyte with high voltage compatibility for all-solid-state batteries, Energy Environ. Sci. 12 (2019) 2665–2671.
[22] J. Liang, X. Li, S. Wang, K.R. Adair, W. Li, Y. Zhao, C. Wang, Y. Hu, L. Zhang, S. Zhao, Site-occupation-tuned superionic Li_xScCl_{3+x} halide solid electrolytes for all-solid-state batteries, J. Am. Chem. Soc. 142 (2020) 7012–7022.
[23] S. Muy, J. Voss, R. Schlem, R. Koerver, S.J. Sedlmaier, F. Maglia, P. Lamp, W.G. Zeier, Y. Shao-Horn, High-throughput screening of solid-state Li-ion conductors using lattice-dynamics descriptors, iScience 16 (2019) 270–282.
[24] R. Schlem, S. Muy, N. Prinz, A. Banik, Y. Shao-Horn, M. Zobel, W.G. Zeier, Mechanochemical synthesis: a tool to tune cation site disorder and ionic transport properties of Li_3MCl_6 (M = Y, Er) superionic conductors, Adv. Energy Mater. 10 (2019), 1903719.
[25] K.H. Park, K. Kaup, A. Assoud, Q. Zhang, X. Wu, L.F. Nazar, High-voltage superionic halide solid electrolytes for all-solid-state Li-ion batteries, ACS Energy Lett. 5 (2020) 533–539.
[26] T. Yu, J. Liang, L. Luo, L. Wang, F. Zhao, G. Xu, X. Bai, R. Yang, S. Zhao, J. Wang, Superionic fluorinated halide solid electrolytes for highly stable Li-metal in all-solid-state Li batteries, Adv. Energy Mater. 11 (2021), 2101915.
[27] Y. Liu, S. Wang, A.M. Nolan, C. Ling, Y. Mo, Tailoring the cation lattice for chloride lithium-ion conductors, Adv. Energy Mater. 10 (2020), 2002356.
[28] S. Wang, Q. Bai, A.M. Nolan, Y. Liu, S. Gong, Q. Sun, Y. Mo, Lithium chlorides and bromides as promising solid-state chemistries for fast ion conductors with good electrochemical stability, Angew. Chem. Int. Ed. 58 (2019) 8039–8043.
[29] N. Adelstein, B.C. Wood, Role of dynamically frustrated bond disorder in a Li^+ superionic solid electrolyte, Chem. Mater. 28 (2016) 7218–7231.
[30] X. Li, J. Liang, X. Yang, K.R. Adair, C. Wang, F. Zhao, X. Sun, Progress and perspectives on halide lithium conductors for all-solid-state lithium batteries, Energy Environ. Sci. 13 (2020) 1429–1461.
[31] J. Liang, X. Li, K.R. Adair, X. Sun, Metal halide superionic conductors for all-solid-state batteries, Acc. Chem. Res. 54 (2021) 1023–1033.
[32] B. Zhang, R. Tan, L. Yang, J. Zheng, K. Zhang, S. Mo, Z. Lin, F. Pan, Mechanisms and properties of ion-transport in inorganic solid electrolytes, Energy Storage Mater. 10 (2018) 139–159.
[33] Z. Lin, T. Liu, X. Ai, C. Liang, Aligning academia and industry for unified battery performance metrics, Nat. Commun. 9 (2018) 5262.
[34] X. Li, J. Liang, K.R. Adair, J. Li, W. Li, F. Zhao, Y. Hu, T.K. Sham, L. Zhang, S. Zhao, Origin of superionic $Li_3Y_{1-x}In_xCl_6$ halide solid electrolytes with high humidity tolerance, Nano Lett. 20 (2020) 4384–4392.
[35] B. Helm, R. Schlem, B. Wankmiller, A. Banik, A. Gautam, J. Ruhl, C. Li, M.R. Hansen, W.G. Zeier, Exploring aliovalent substitutions in the lithium halide superionic conductor $Li_{3-x}In_{1-x}Zr_xCl_6$ ($0 \le x \le 0.5$), Chem. Mater. 33 (2021) 4773–4782.
[36] D. Chen, S. Li, J. Jie, S. Li, S. Zheng, M. Weng, C. Yu, S. Li, D. Chen, F. Pan, A descriptor of "material genes": effective atomic size in structural unit of ionic crystals, Sci. China Technol. Sci. 62 (2019) 849–855.
[37] J. Jie, M. Weng, S. Li, D. Chen, S. Li, W. Xiao, J. Zheng, F. Pan, L. Wang, A new MaterialGo database and its comparison with other high-throughput electronic structure databases for their predicted energy band gaps, Sci. China Technol. Sci. 62 (2019) 1423–1430.
[38] J. Zheng, Y. Ye, F. Pan, 'Structure units' as material genes in cathode materials for lithium-ion batteries, Natl. Sci. Rev. 7 (2020) 242–245.
[39] G. Kresse, J. Hafner, Ab initio molecular-dynamics simulation of the liquid-metal-amorphous-semiconductor transition in germanium, Phys. Rev. B 49 (1994) 14251.
[40] G. Kresse, D. Joubert, From ultrasoft pseudopotentials to the projector augmented-wave method, Phys. Rev. B 59 (1999) 1758.
[41] S.P. Ong, W.D. Richards, A. Jain, G. Hautier, M. Kocher, S. Cholia, D. Gunter, V.L. Chevrier, K.A. Persson, G. Ceder, Python Materials Genomics (pymatgen): a robust, open-source python library for materials analysis, Comput. Mater. Sci. 68 (2013) 314–319.
[42] H. Chen, L.L. Wong, S. Adams, SoftBV–a software tool for screening the materials genome of inorganic fast ion conductors, Acta Crystallogr. B: Struct. Sci. Cryst. Eng. Mater. 75 (2019) 18–33.
[43] Z. Hu, M. Weng, Z. Chen, W. Tan, S. Li, F. Pan, The role of $M@Ni_6$ superstructure units in honeycomb-ordered layered oxides for Li/Na ion batteries, Nano Energy 83 (2021), 105834.
[44] D. Park, H. Park, Y. Lee, S.O. Kim, H.G. Jung, K.Y. Chung, J.H. Shim, S. Yu, Theoretical design of lithium chloride superionic conductors for all-solid-state high-voltage lithium-ion batteries, ACS Appl. Mater. Interfaces 12 (2020) 34806–34814.
[45] R. Xiao, H. Li, L. Chen, High-throughput design and optimization of fast lithium ion conductors by the combination of bond-valence method and density functional theory, Sci. Rep. 5 (2015) 1–11.
[46] B. Zhang, J. Zhong, Y. Zhang, L. Yang, J. Yang, S. Li, L.W. Wang, F. Pan, Z. Lin, Discovering a new class of fluoride solid-electrolyte materials via screening the structural property of Li-ion sublattice, Nano Energy 79 (2021), 105407.
[47] A. Van der Ven, Z. Deng, S. Banerjee, S.P. Ong, Rechargeable alkali-ion battery materials: theory and computation, Chem. Rev. 120 (2020) 6977–7019.
[48] J. Huang, P. Zhong, Y. Ha, D.-H. Kwon, M.J. Crafton, Y. Tian, M. Balasubramanian, B.D. McCloskey, W. Yang, G. Ceder, Non-topotactic reactions enable high rate capability in Li-rich cathode materials, Nat. Energy 6 (2021) 706–714.
[49] J. Lee, A. Urban, X. Li, D. Su, G. Hautier, G. Ceder, Unlocking the potential of cation-disordered oxides for rechargeable lithium batteries, Science 343 (2014) 519–522.
[50] F. Chen, S. Cheng, J.B. Liu, S. Li, W. Ouyang, B. Liu, Insights into the electrochemical stability and lithium conductivity of Li_4MS_4 (M= Si, Ge, and Sn), ACS Appl. Mater. Interfaces 13 (2021) 22438–22447.
[51] W. Xiao, C. Xin, S. Li, J. Jie, Y. Gu, J. Zheng, F. Pan, Insight into fast Li diffusion in Li-excess spinel lithium manganese oxide, J. Mater. Chem. A 6 (2018) 9893–9898.